Chem

CellPress

Article

Propane Dehydrogenation on Single-Site [$PtZn_4$] Intermetallic Catalysts

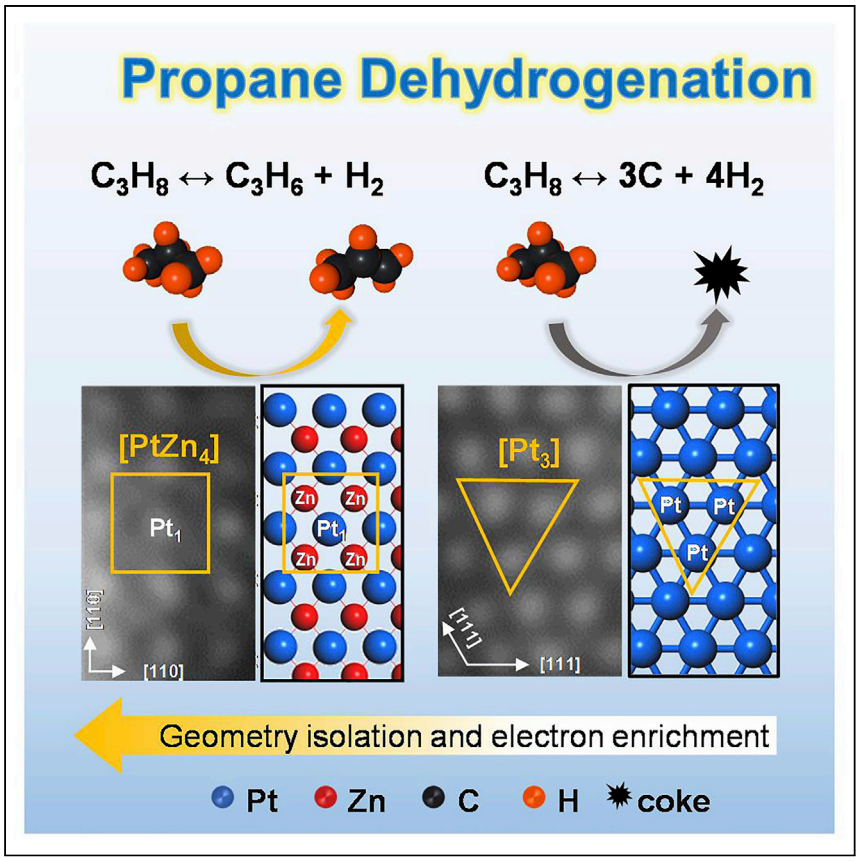

This paper describes single-site intermetallic catalysts for propane dehydrogenation.

Sai Chen, Zhi-Jian Zhao, Rentao Mu, ..., Evgeny Vovk, Yong Yang, Jinlong Gong

jlgong@tju.edu.cn

HIGHLIGHTS

Constructing selective and ultrastable single-site intermetallic catalysts

Achieving the highest propylene productivity at the lowest deactivation rate

Revealing active site structures under representative dehydrogenation reaction

Chen et al., Chem 7, 387–405
February 11, 2021
https://doi.org/10.1016/j.chempr.2020.10.008

Chem

CellPress

Article

Propane Dehydrogenation on Single-Site [$PtZn_4$] Intermetallic Catalysts

Sai Chen,[1,2] Zhi-Jian Zhao,[1,2] Rentao Mu,[1,2] Xin Chang,[1,2] Jun Luo,[3] Stephen C. Purdy,[4] A. Jeremy Kropf,[5] Guodong Sun,[1,2] Chunlei Pei,[1,2] Jeffrey T. Miller,[4] Xiaohong Zhou,[6] Evgeny Vovk,[6] Yong Yang,[6] and Jinlong Gong[1,2,7,8,*]

SUMMARY

Propane dehydrogenation (PDH) is a commercial propylene production technology that has received much attention, but high reaction temperatures result in a decrease of propylene selectivity and catalyst stability. This paper describes a single-site [$PtZn_4$] catalyst by assembling atomically ordered intermetallic alloy (IMA) as a selective and ultrastable PDH catalyst. The catalyst enables more than 95% of propylene selectivity from 520°C to 620°C. No obvious deactivation is observed within the 160-h test, superior to $PtSn/Al_2O_3$ and state-of-the-art Pt-based catalysts. Based on *in situ* X-ray absorption fine structure, X-ray photoelectron spectroscopy measurements, and density functional theory calculations, we reveal that the surface [$PtZn_4$] ensembles in PtZn IMAs serve as the key active site structures, wherein the geometry-isolated and electron-rich Pt_1 site in [$PtZn_4$] ensembles readily promotes the first and second C–H cleavage of propane but inhibits further dehydrogenation of surface-bounded propylene. This significantly improves the selectivity and stability by prohibiting coke side reactions.

INTRODUCTION

A change of feedstock from naphtha to light alkanes, due to the emergence of shale gas and the increasing availability of natural gas, has led to an increasing development of on-purpose propane dehydrogenation (PDH) technologies.[1–3] PDH is an extremely energy-intensive process largely due to the high positive enthalpy of the reactions ($\Delta_r H^\circ$ = 124 kJ mol^{-1}), necessitating high reaction temperatures,[4–6] which presents grand challenges for alkene selectivity and catalyst stability.[7] Especially, it has been shown that larger ensembles of active sites catalyze structure-sensitive side reactions, including cracking and deep dehydrogenation, leading to the production of C_1 and C_2 molecules and coke.[8]

To tackle these challenges, the "active site isolation" strategy has been proved to be effective.[9–11] Isolating the active metal components into the single-atom site and the resulting single-atom catalysts (SACs) could inhibit the structure-sensitive side reactions.[2,9,12–15] For example, the isolated Pt_1 site in Pt/Cu single-atom alloy (SAA) can only interact with a single Pt atom for the deep dehydrogenated C_3H_5, a model precursor of coke formation, instead of three more stable Pt–C interactions on a 3-fold Pt_3 hollow site over Pt (111), leading to less carbon deposition. However, the long-term stability of Pt/Cu SAAs is disillusionary due to its thermal and chemical instabilities.[9,16,17] Although single-site Zn(II),[18] Co(II),[19] Ni(II),[20] and Ga(III)[21] on silica have been developed, these active sites suffer from low intrinsic activity and reduction

The Bigger Picture

Propane dehydrogenation (PDH) is a commercial propylene production technology, but high reaction temperatures result in cracking and coking. Isolating active metal components into single atoms can maximize atomic efficiency, and the resulting single-atom catalysts (SACs) could inhibit structure-sensitive side reactions with unprecedented selectivity.

Herein, we report a single-site [$PtZn_4$] catalyst by assembling atomically ordered PtZn intermetallic alloys, which enables more than 95% selectivity of propylene over a broad temperature range of 520°C to 620°C. No obvious deactivation is observed within the 160-h industrial PDH test. We reveal that the surface [$PtZn_4$] ensembles in PtZn IMAs serve as the stable active site structures, wherein the geometry-isolated and electron-rich Pt in [$PtZn_4$] ensembles readily promotes desorption of surface-bounded propylene and improves the stability by prohibiting coke side reactions.

deactivation. The development of highly efficient and stable SACs, therefore, remains grand challenges in the field of alkane dehydrogenation at elevated temperatures.

Atomically ordered Pt_1M_1 intermetallic alloy (IMA) (molar ratio of Pt/M = 1) contains one active metal Pt and another inert component M, which can disperse the active sites into the isolated Pt_1 site by the neighboring M atoms.[11,22,23] Additionally, this highly ordered crystalline structure provides active sites with higher thermal stability compared with conventional single-atom alloys.[11] For example, PtZn IMA has been reported in ethane dehydrogenation.[24] However, the loading of Pt is relatively high with about 9.53 wt %, which is far higher than that of the industrial Pt-based catalysts with the Pt loading of about 0.3 wt % in $PtSn/Al_2O_3$. This induces low olefin productivity and atom utilization. Recently, novel preparation methods have been developed to improve the propylene productivity by constructing ultrasmall PtZn bimetal nanoclusters by embedding them inside S-1 zeolites.[25,26] However, due to the very complex coordination structures in zeolites, e.g., the coexistence of Pt–O, Pt–Pt, and Pt–Zn coordinations, it is very difficult to identify the active site structures, regardless of experimental and theoretical simulations. Therefore, further revealing the unclear active site structures and promoting propylene productivity is highly desired.

This paper describes a selective and ultrastable single-site $[PtZn_4]$ catalyst by assembling atomically ordered PtZn IMA with trace Pt loadings of 0.1 wt %, which enables more than 95% selectivity of propylene over a broad temperature range of 520°C to 620°C and the highest propylene productivity of 83.2 mol C_3H_6 g_{Pt}^{-1} h^{-1}. No obvious deactivation was observed within 160-h under industrial operating conditions, superior to $PtSn/Al_2O_3$ and state-of-the-art Pt-based catalysts. Based on *in situ* X-ray absorption fine-structure spectroscopy measurements, X-ray photoelectron spectroscopy measurements, and density functional theory calculations, it is further revealed that surface $[PtZn_4]$ ensembles in $Pt1Zn_1$ (110) serve as the stable active site structures, wherein the geometry-isolated and electron-rich Pt in $[PtZn_4]$ ensembles readily promote desorption of the surface-bounded propylene and improve the stability by prohibiting coke formation and segregation of Pt and Zn atoms via structural ordering.

RESULTS

Formation of Single-Atom Pt_1 Sites in PtZn IMAs

By direct H_2 temperature-programmed reduction strategy (see Experimental Procedures), we successfully constructed PtZn IMAs (molar ratio of Pt:Zn = 1) supported on SiO_2, where the H_2-rich atmosphere at high temperatures (HT) of 600°C contributes to the transformation of disordered PtZn nanoparticles (NPs) into structurally ordered PtZn IMAs (Figure 1A).[27] We monitored the formation and transformation from Pt to PtZn IMAs by X-ray diffraction (XRD) patterns at different reduction temperatures (Figure S1). After 600°C reduction, a set of new diffraction peaks (31.1°, 40.8°, and 44.8°) appeared, which are ascribed to (110), (111), and (200), respectively, corresponding well with the standard PXRD patterns (PDF#06-0604) of intermetallic Pt_1Zn_1 (P4/mmm) (Figure 1C).[24,27] This is definitely different from the diffraction peaks (39.8°, 46.2°), which are ascribed to (111) and (200) of Pt (Fm3m) (PDF#04-0802). Notably, the crystalline phase has been transformed from the face-centered cubic (fcc) of Pt to body-centered tetragonal (bct) Pt_1Zn_1 IMA (Figure 1B). The average particle sizes of 0.1Pt0.17Zn alloy (additions of 0.1 wt % Pt and 0.17 wt % Zn) supported on SiO_2 significantly decreased from 2.1 nm ($0.1Pt/SiO_2$, additions

[1]Key Laboratory for Green Chemical Technology of Ministry of Education, School of Chemical Engineering & Technology, Tianjin University, Tianjin 300072, China

[2]Collaborative Innovation Center for Chemical Science & Engineering (Tianjin), Tianjin 300072, China

[3]Center for Electron Microscopy, Institute for New Energy Materials and Low-Carbon Technologies, School of Materials, Tianjin University of Technology, Tianjin 300384, China

[4]Davidson School of Chemical Engineering, Purdue University, West Lafayette, IN 47907, USA

[5]Chemical Sciences and Engineering Division, Argonne National Laboratory, Lemont, IL 60439, USA

[6]School of Physical Science and Technology, ShanghaiTech University, Shanghai 201210, China

[7]Joint School of National University of Singapore and Tianjin University, International Campus of Tianjin University, Binhai New City, Fuzhou 350207, China

[8]Lead Contact

*Correspondence: jlgong@tju.edu.cn

https://doi.org/10.1016/j.chempr.2020.10.008

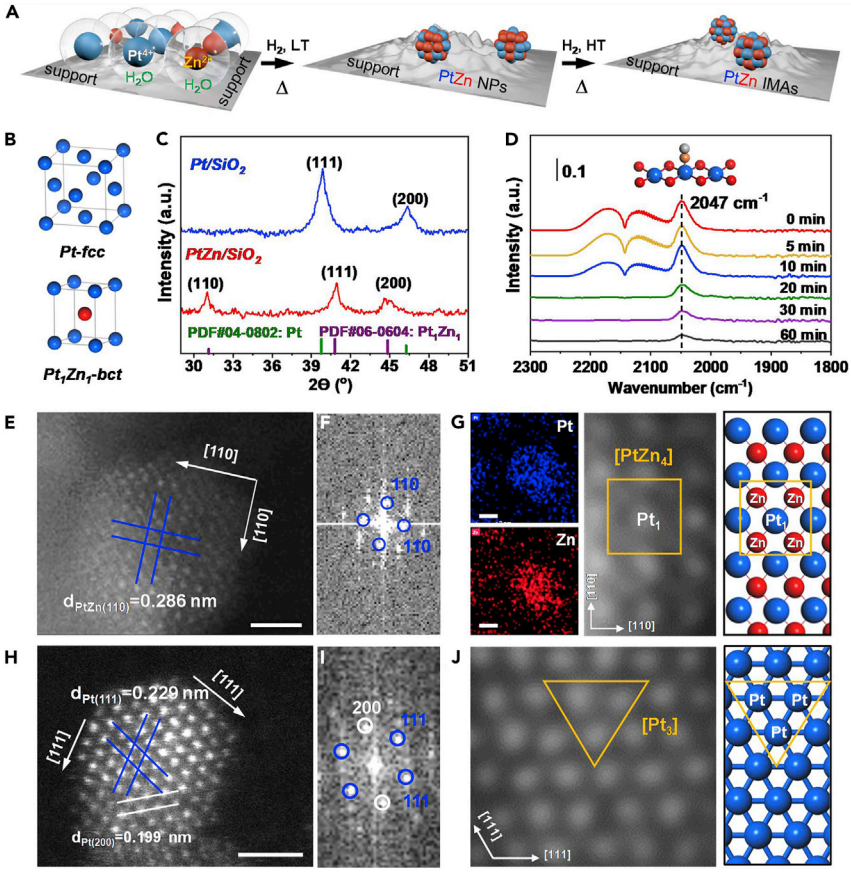

Figure 1. Formation of Single-Atom Pt_1 Site in PtZn IMAs

(A) Schematic illustration of high-temperature H_2 reduction to form ordered PtZn IMAs on SiO_2.

(B) Crystal structures of Pt and PZn IMA (Pt, blue; Zn, red).

(C) XRD patterns of 1Pt/SiO_2 and 1Pt1.7Zn/SiO_2.

(D) CO-DRIFTS of 0.1Pt0.17Zn/SiO_2 IMAs.

(E) AC-HAADF-STEM images of 1Pt1.7Zn/SiO_2. The scale bar is 1 nm.

(F) FFT image of the PtZn particle in (E).

(G) EDS mapping images enlarged AC-HAADF-STEM image of 1Pt1.7Zn/SiO_2 and DFT simulated structure of PtZn (110) (Pt, blue; Zn, red).

(The framed rectangular represents the surface [$PtZn_4$] ensemble, wherein single-atom Pt_1 sites forms)

(H) AC-HAADF-STEM images of 1Pt/SiO_2. The scale bar is 1 nm.

(I) FFT image of the Pt particle in (H).

(J) Enlarged AC-HAADF-STEM image of 1Pt/SiO_2 and DFT simulated structure of Pt (111) (Pt, blue).

(The framed triangle represents the [Pt_3] ensemble)

of 0.1 wt % Pt) to 0.9 nm due to the ensemble effect between Pt and Zn atoms (Figure S2). Aberration-corrected high-angle annular dark-field scanning transmission electron microscope (AC-HAADF-STEM) imaging (Figure 1E and S3) revealed the formation of atomically ordered PtZn IMAs, featuring the alternating bright Pt column and dark Zn column contrast on [110] planes (Figure 1E). Energy dispersive spectrometry (EDS) elemental mappings of the PtZn nanoparticle indicated the homogeneous distribution of Pt and Zn atoms (Figure 1G) with an approximately 1:1 ratio. Considering that the Zn content in this PtZn nanoparticle is lower than those fed in the catalyst (1 wt % Pt and 1.7 wt % Zn), a part of Zn may present on SiO_2 support. The fast Fourier transform (FFT) image of the PtZn nanoparticle in Figure 1E shows the superlattice diffraction patterns, which further implies the formation of

ordered Pt_1Zn_1 IMAs (Figure 1F). The atomic plane distances were measured as 0.286 nm, agreeing with a lattice spacing of intermetallic Pt_1Zn_1 along with the [110] directions, which implies the highly exposed (110) facets in these PtZn IMAs. At the surface of PtZn (110), the [$PtZn_4$] ensembles (rectangle-framed motif) periodically formed, in which Pt atom was isolated by 4 neighboring Zn atoms, leading to the formation of single-atom Pt_1 site. Comparatively, for Pt/SiO_2, AC-HAADF-STEM imaging (Figure S4) showed that two atomic plane distances were measured as 0.229 and 0.199 nm (Figure 1H), which were in agreement with the lattice spacing along the [111] and [200] directions. On the surface of Pt (111), the [Pt_3] ensembles (triangle-framed motif) periodically formed (Figure 1J), indicating the formation of surface Pt_3 sites over Pt/SiO_2.

To further obtain information about different surface Pt ensembles over Pt/SiO_2 and $PtZn/SiO_2$, we performed Fourier transform infrared (FTIR) spectroscopy with CO adsorption. For Pt/SiO_2, one CO adsorption peak appeared in CO-diffuse reflectance infrared Fourier transform spectroscopy (DRIFTS) (Figure S5) at 2,075 cm^{-1}, which was assigned to stretching vibration of CO adsorbed on Pt ensembles with on-top modes. Comparatively, for $PtZn/SiO_2$, upon the increase of reduction temperatures, the CO adsorption band corresponding to Pt ensembles (2,075 cm^{-1}) disappeared with an appearance of a new band feature at around 2,047 cm^{-1} (Figure S6). Noticeably, no position changes of this band was observed with the decrease of CO coverage during the 60 min purge (Figure 1D), indicating that the band at 2,047 cm^{-1} might have been assigned to the on-top CO adsorbed on the single-atom Pt_1 site.[28,29] These results clearly demonstrate the formation of a single-atom Pt_1 site in PtZn IMAs supported on SiO_2.

Catalytic Performance and Stability

Kinetic studies of the catalysts showed that H_2 response in terms of the rate-determining initial C–H cleavage in C_3H_8 temperature-programmed surface reaction (TPSR) starts at about 181°C on Pt/SiO_2, 214°C on $PtZn/SiO_2$, and 500°C on Zn/SiO_2, respectively (Figure S7), revealing that the Pt atom might serve as the active component and Zn functions as the promoter, which slightly increases the C–H activation temperature. The formation of CH_4 as a result of cracking and coke side reactions at HT was significantly inhibited with the addition of Zn over $PtZn/SiO_2$, which might signify the higher propylene selectivity and anti-coke resistance. According to Pt dispersions (Figure S8) and specific activity at 600°C, the calculated turnover frequency $(TOF)_{C3H6}$ (6.8 s^{-1}) over $PtZn/SiO_2$ was much higher than that over Pt/SiO_2 (4.6 s^{-1}) (Table S1), suggesting the superior ability of propylene production over $PtZn/SiO_2$ than Pt/SiO_2.

When testing for PDH, we evaluated the influence of Pt and Zn additions, H_2 pressures, weight hourly velocity (WHSV) of propane, and reaction temperatures on propane conversion and propylene selectivity. As a result, increasing Zn additions and H_2 pressures contribute to the improvement of propylene selectivity (Figures S9 and S10). Increasing Pt loadings (Figure S11) and reaction temperatures (Figure S12) increases the conversion of propane, while higher WHSV of propane (Figure S13) leads to the loss of conversion. Optimally, the $PtZn/SiO_2$ with a low loading of 0.1 wt % Pt and 0.17 wt % Zn obtained about 48% of propane conversion and 96% of propylene selectivity at 600°C and WHSV of propane = 4 h^{-1} (C_3H_8/H_2 = 1/1), which is significantly higher than that over Pt/SiO_2 (42% conversion, 67% selectivity) (Figure 2A) and Zn/SiO_2 (4% conversion, 60% selectivity) (Figure S14). In addition, supports could influence the structures of PtZn alloys and thus dehydrogenation performance. We found that PtZn supported on SiO_2 exhibited better both propane conversion

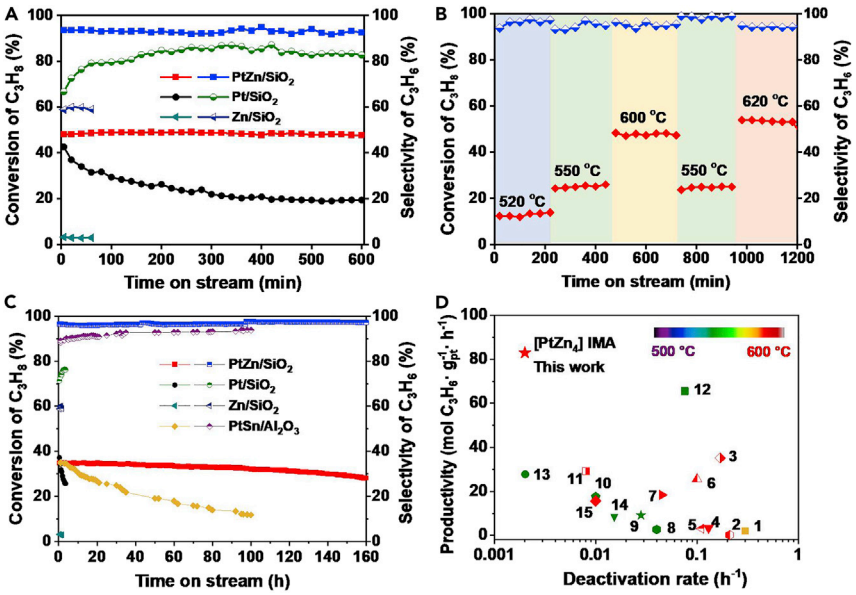

Figure 2. Catalytic Performance and Stability Test

(A) Propane conversion and propylene selectivity as a function of reaction time over the prepared 0.1Pt/SiO_2, 0.1Pt0.17Zn/SiO_2 IMA and 0.17Zn/SiO_2 at 600°C. Catalytic conditions: atmospheric pressure, C_3H_8/H_2 = 1/1, with balance N_2 for a total flow rate of 50 mL min^{-1}, WHSV of propane = 4 h^{-1}, and 250 mg of sample.

(B) Propane conversion and propylene selectivity over the prepared 0.1Pt0.17Zn/SiO_2 IMA ranging from 520°C to 620°C. Catalytic conditions: atmospheric pressure, C_3H_8/H_2 = 1/1, with balance N_2 for total flow rate of 50 mL min^{-1}, WHSV of propane = 4 h^{-1} and 250 mg of sample.

(C) Stability test as a function of reaction time over the prepared 0.1Pt/SiO_2, 0.1Pt0.17Zn/SiO_2 IMA, 0.17Zn/SiO_2 and PtSn/Al_2O_3 at 600°C. Catalytic conditions: atmospheric pressure, C_3H_8/H_2 = 2/1, total flow rate 12 mL min^{-1}, no N_2 dilution, WHSV of propane = 11 h^{-1} and 100 mg of sample.

(D) Productivity of C_3H_6 versus deactivation rate for the catalysts described in this work and literature (1–15, see Table S2). The catalysts included here are only the best-performing ones from the articles considered.

and propylene selectivity than Al_2O_3 (Figure S15), despite the similar sizes of PtZn particles (Figure S16). The reason may be that SiO_2 interacts weakly with the metals, allowing for a greater extent of metal interaction and alloying between Pt and Zn, which may be the significant support effect for the IMA formation.[22,30] Consequently, there was a lower CO adsorption band position (2,047 cm^{-1}) over PtZn/SiO_2 than that over PtZn/Al_2O_3 (2,069 cm^{-1}) (Figure S5). Additionally, the stronger acidity of Al_2O_3 supports than SiO_2 (Figure S17A) would lead to coking and catalyst deactivation. Raman spectra of the spent catalysts (Figures S17B and S17C) further indicated that the coke amount and graphitization degree (the calculated ratio of I_D/I_G) of PtZn/SiO_2 was significantly lower than that over PtZn/Al_2O_3. Therefore, the weak acid SiO_2 in this work was selected as a support to promote the formation of highly alloying PtZn IMA and suppress the influence of support acidity on coking behaviors.

Consequently, SiO_2-supported PtZn IMAs showed ascendant temperature tolerance ranging from 520°C to 620°C, enabling over 95% selectivity of C_3H_6 (Figure 2B), indicating superior selectivity of this PtZn IMA during the wide range of HTs. Moreover, the PtZn IMA catalysts ran more than 160 and 100 h of continuous operation with little deactivation at 520°C (Figure S18) and 575°C (Figure S19), respectively. To further evaluate the stability of this PtZn IMA catalyst, we performed the long-term test under industrial operating conditions (600°C, WHSV of C_3H_8=11 h^{-1}, C_3H_8/

H_2 = 2, no inert gas dilution) and compared with the representative $PtSn/Al_2O_3$ catalysts (see Experimental Procedures). After 160 h, dehydrogenation reaction showed a very slight decrease in the conversion of 0.04% per hour, suggesting that only slight deactivation had occurred. Meanwhile, the propylene selectivity was as high as 97.2% after a 160-h test (Figure 2C). In contrast, for the $PtSn/Al_2O_3$ reference catalyst, propane conversion dramatically dropped from an initial 34.8% to 11.7% after 100 h. A first-order deactivation model was used to evaluate the catalyst stability (for details, see Experimental Procedures).[28] A comparatively lower deactivation rate of 0.002 h^{-1} and a catalyst lifetime of 160 h for the $PtZn/SiO_2$ IMA quantitatively demonstrate its high stability compared with the $PtSn/Al_2O_3$ catalyst (0.01 h^{-1}, 100 h). The highest productivity of 83.2 mol C_3H_6 g_{Pt}^{-1} h^{-1}, more than 5 times of $PtSn/Al_2O_3$ catalysts, at the lowest deactivation rate (0.002 h^{-1}) clearly demonstrates the superior reactivity and stability of the $PtZn/SiO_2$ IMA catalyst in the PDH reaction, which is superior to $PtSn/Al_2O_3$ and those of state-of-the-art Pt-based catalysts (Figure 2D; Table S2). Additionally, during 4 successive regeneration cycles, the propane conversion and propylene selectivity remained slightly changed as compared with the initial run (Figure S20), further indicating the good regenerability of this PtZn IMA.

PtZn IMAs under PDH Conditions

To further investigate the stability of PtZn IMA catalysts under PDH reaction conditions, *in situ* X-ray absorption near-edge structure (XANES) spectra and Fourier transforms (FTs) of the extended X-ray absorption fine-structure (EXAFS) spectra were collected.

As shown in Figure 3A, after H_2 reduction, all Pt atoms were in their metallic states, as evidenced by the white line intensity relative to that of the Pt foil. The edge energy of the $PtZn/SiO_2$ was shifted to 11,565 eV, indicating the formation of bimetallic PtZn particles. Additionally, *in situ* Pt L_{III} EXAFS revealed a single broad peak in R space centered around 2.2 Å in $PtZn/SiO_2$, whereas Pt/SiO_2 showed three peaks in R space, characteristic of Pt–Pt scattering (Figures 3B and S21). For $PtZn/SiO_2$ catalysts, the model gave high quality fits with the crystal structure of the β_1-Pt_1Zn_1 IMA. The FT peak at 2.57 Å could be unambiguously ascribed to Pt–Zn coordination whose number (CN) was determined to be about 4 (Table S3) lower than the values (8 zinc neighbors and 4 Pt neighbors) in bulk PtZn IMA. This is consistent with the consensus that intrinsically stable single-atom site is usually formed by 4 coordinate complexes containing a metal with tetrahedral or square-planar coordination geometry. Considering the under coordinated surface atoms in this sub-1 nm PtZn IMA particle, the surface coordination of Pt–Zn ensembles could be approximately identified as this obtained coordination environment of $[PtZn_4]$ ensembles.[17,31] Therefore, as the illustrations shown in Figure S22, the $[PtZn_4]$ coordination structure exists on the surface of PtZn IMAs, wherein single-atom Pt_1 site forms and it is isolated by 4 neighboring Zn atoms in $[PtZn_4]$ ensembles. Notably, the XANES and EXAFS spectra of $PtZn/SiO_2$ under PDH reaction conditions are similar with H_2 reduction (Figures 3C and S23), and the calculated CN of Pt–Zn remained about 4 (Table S3), indicating the superior stability of PtZn coordination ensembles in PtZn IMAs under PDH reaction conditions.

In situ X-ray photoelectron spectroscopy (XPS) was further employed to monitor the electronic states of this PtZn ensembles. After H_2 reduction, for $PtZn/SiO_2$, Pt was reduced to metallic Pt^0 and the binding energy (BE) of Pt^0 in Pt $4f_{7/2}$ peak was 71.1 eV (Figures 3D and S24), which was lower than that over Pt/SiO_2 (71.3 eV) (Figure S25), indicating the electron transfers from Zn to the 5d band of Pt and formation

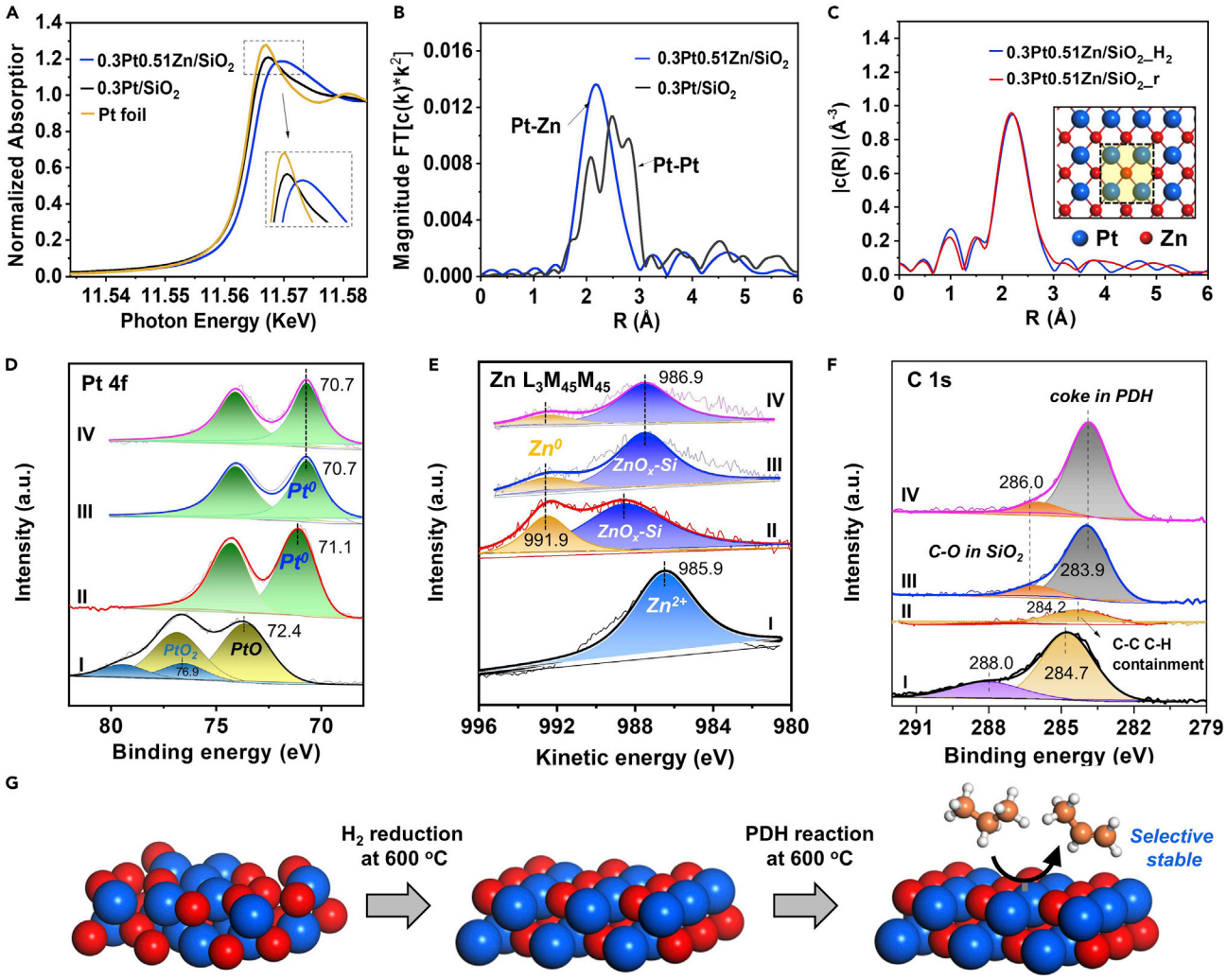

Figure 3. ***In Situ*** **XAFS and XPS Measurements of Stable [$PtZn_4$] Ensembles under PDH Conditions**

(A) *In situ* Pt L_{III} edge XANES spectra of Pt/SiO_2 and PtZn/SiO_2 IMA after H_2 reduction.

(B) *In situ* Pt L_{III} edge EXAFS spectra of Pt/SiO_2 and PtZn/SiO_2 IMA after H_2 reduction.

(C) *In situ* Pt L_{III} edge EXAFS spectra of PtZn/SiO_2 IMA. H_2 and r represent the samples under H_2 reduction and PDH reaction, respectively.

(D) *In situ* XPS spectra of Pt 4f in 0.1Pt0.17Zn/SiO_2 IMA.

(E) *In situ* XPS spectra of Zn 2p and Zn LMM in 0.1Pt0.17Zn/SiO_2 IMA.

(F) *In situ* XPS spectra of C 1s in 0.1Pt0.17Zn/SiO_2 IMA.

(I–IV denote the fresh samples, the samples after H_2 reduction, the samples after C_3H_8 reaction at 600°C for 30 min and 60 min, respectively)

(G) Illustration of structure evolution of [$PtZn_4$] catalysts during H_2 pretreatment (0.1Pt0.17Zn/SiO_2_H_2) and PDH reactions (0.1Pt0.17Zn/SiO_2_r).

of electron-rich Pt in PtZn ensembles.[24,32] Combining spectra of Zn 2p and Zn LMM Auger (Figures 3E and S26), it was found that Zn^{2+} species (985.9 eV) were partially reduced to metallic Zn^0 (991.9 eV) and some nonreducible ZnO_x. Therefore, we infer that partial Zn species are alloyed with Pt to form PtZn alloys, while some nonreducible ZnO_x species strongly interact with SiO_2 supports to form ZnO_x-Si (ZnO_x bridging with SiO_2 support, 986.9 eV). Through peak fitting, the percent of surface composition of Zn^0 and ZnO_x-Si were calculated to be 30.3% and 69.7%, respectively. Based on atomic concentration quantitative analysis (Table S4) and the peak fitting of Zn^0 and ZnO_x-Si, the molar ratio of Zn^0/Pt^0 in this PtZn IMA catalyst was accordingly determined to be 1.4, which is close to the ratio of Pt and Zn atoms in $Pt1Zn_1$ IMA (molar ratio of Pt:Zn = 1:1). Under PDH conditions, there was a slightly

negative shift of Pt $4f_{7/2}$ peaks over PtZn/SiO_2 (from 71.1 to 70.7 eV) (Figure 3D) and Pt/SiO_2 (from 71.3 to 70.9 eV) (Figure S25), which may be induced by the affinity of coke deposition on the surface of Pt^0 sites. Comparatively, there was no obvious position change of the Zn^0 peak in Zn LMM. Additionally, both the intensities of Pt^0 and Zn^0 was slightly decreased due to the cover of coke on the surface of PtZn alloys. Therefore, Pt^0 in PtZn ensembles may be the main coking site. Consequently, for Pt/SiO_2, a more pronounced intensity of coke deposition (283.9 eV) in XPS C 1s peak (Figure S27) than that over PtZn/SiO_2 (Figure 3F) was observed. Therefore, the above results clearly imply that the electron-rich Pt in PtZn ensembles effectively inhibits the coke formation under PDH reaction conditions.

To further shed light on the reason for the inhibited coke over PtZn ensembles, C_3H_6-temperature-programmed desorption (TPD) and C_3H_6-IR were operated to investigate the relationship between C_3H_6 intermediate adsorption, which determines the coke formation. As C_3H_6-TPD profiles shown in Figure S28A, there was a very weak desorption peak at 261°C for PtZn/SiO_2 compared with the strong desorption peak at 287°C for Pt/SiO_2, indicating that the interaction between C_3H_6 molecules and Pt sites was weaker over PtZn/SiO_2 than that over Pt/SiO_2. This weak interaction minimizes the adsorption of C_3H_6 on the electron-rich Pt sites in PtZn ensembles, which therefore accounts for higher propylene selectivity and less coke formation over PtZn/SiO_2. For C_3H_6-IR (Figure S28B), it is was also obviously indicated that the C_3H_6 adsorption was weakened on the surface of PtZn/SiO_2, since a lower uptake of propylene was presented, which suggests that PtZn ensembles effectively facilitate propylene desorption. As a result, DRIFTS of CO on PtZn/SiO_2 with an increase in reaction time showed that there were no obvious position and intensity changes of CO adsorption band, indicating its superior ability of propylene desorption and anti-coking resistance (Figure S29A). In contrast, for Pt/SiO_2, the peak position of CO adsorption gradually shifted to the lower wavenumber, from 2,076 to 2,047 cm^{-1} at 10 h (Figure S29B). Also, the intensity of CO adsorption gradually decreased with reaction time, which may be caused by the much severe coke depositing on the highly unsaturated corner or steps sites of Pt atoms in Pt/SiO_2, leading to the red-shift and weakening of CO adsorption band.[28] Additionally, the coking amount on the spent PtZn/SiO_2 (2.1%) was much lower than that on Pt/SiO_2 (Figure S30), which corresponds to the less coke formation on PtZn/SiO_2 than that over Pt/SiO_2, as shown in temperature-programmed oxidation (TPO) profiles (Figure S31). Raman spectra further detected the difference of coke type in addition to the coke amount. With reaction time, two distinct Raman bands at around 1,602 and 1,321 cm^{-1} were observed (Figure S32A), ascribed to coke G (graphite) and D (disorder) modes, respectively. The calculated ratio of I_D/I_G from spent PtZn/SiO_2 was determined to be 1.3, much higher than that overspent Pt/SiO_2 (I_D/I_G =0.6) (Figure S32B), indicating the lower graphitization degree of coke deposited on this PtZn ensemble than Pt, in addition to less coke amount.

Besides coke deposition, particle sintering and component loss are other main reasons for catalyst deactivation.[9] Transmission electron microscope (TEM) analysis showed that the size of spent PtZn/SiO_2 (1.0 nm) had undergone negligible changes (Figure S33), indicating that the PtZn particles show superior anti-sintering resistance during PDH reactions due to the intrinsically high thermal stability of PtZn IMAs. Additionally, the crystalline structure of PtZn alloys is almost unchanged even after long-term stability tests (Figure S34). Furthermore, inductively coupled plasma optical emission spectroscopy (ICP-OES) component analysis as a function of time on stream implies very slight loss rates of Zn and Pt in PtZn/SiO_2 (Table S5; Figure S35), far lower than that over Zn/SiO_2, Pt/SiO_2, and other Zn promoted Pt-based

catalysts.[32,33] In addition, after continuous regeneration processes, the PtZn IMAs maintained its initial crystalline structure, pore distribution, and particle size (~1.1 nm) (Figure S36; Table S6), indicating the good regenerability of this PtZn IMA catalyst.

Therefore, by analyzing the coke, particle sintering, and component loss, as shown in Figure 3G, we reasonably consider that the PtZn ensembles in PtZn IMAs exhibit superior anti-coking capacity and stability under PDH reactions conditions.

[$PtZn_4$] Ensembles as the Key Active Site Structures

The above experimental characterizations have evidenced the formation of single-atom Pt_1 sites inside [$PtZn_4$] ensembles, which keep stable under PDH conditions.[24,27] To further investigate the surface-active structures, we have quantified the mole amounts of surface [$PtZn_4$] species over different PtZn IMAs (0.1Pt0.17Zn/SiO_2, 0.3Pt0.51Zn/SiO_2, 0.5Pt0.85Zn/SiO_2, and 1Pt1.7Zn/SiO_2) with different particle sizes by altering the additions of Pt and Zn with fixed molar ratios of Pt and Zn. The HADDF-STEM images (Figure S37) showed that as the Pt loadings increased from 0.1 to 1 wt %, the mean sizes of PtZn particles have gradually increased from 0.9 to 2.2 nm. *In situ* EXAFS spectra (Figures 4A and S38) showed that the different PtZn/SiO_2 samples exhibit the same single broad peak in R space centered around 2.2 Å and the model gave high quality fits to the Pt_1Zn_1 IMA phase. The Pt–Zn and Pt–Pt coordination numbers were lower than the bulk values due to the large fraction of under coordinated surface atoms (Table S3). For the same reason, the Pt–Pt, and Pt–Zn bond distances were contracted from that of the bulk value for Pt_1Zn_1, with the contraction becoming more pronounced as the Pt loadings decreased. This is consistent with the particle size decreasing with the Pt loadings. Therefore, the different PtZn/SiO_2 samples exhibit the same crystalline structures of intermetallic Pt_1Zn_1. The density functional theory (DFT) calculation of the comparison of surface energies of low-index surfaces of (110), (111), and (200) shows that (110) surface has the lowest surface energy, which indicates that the (110) surface is the most stable (Table S7). Considering the facet of (110) as the most stable plane, it would prefer to expose on the surface of Pt_1Zn_1 IMAs. On the surface of (110), each Pt atom is coordinated with 4 neighboring Zn atoms and forms the [$PtZn_4$] ensembles (Figure S22). Therefore, the amount of [$PtZn_4$] species are approximately equal the amount of surface-exposed Pt atoms, which can be determined by the dispersion of Pt atoms. As shown in Figure S39, with the increasing of Pt loadings from 0.1 to 1 wt % and particle sizes from 0.9 to 2.2 nm, the dispersion of Pt atoms correspondingly decreases from 88.3% to 36.1%. Notably, under PDH reactions, we found that these different PtZn/SiO_2 samples exhibited very close propylene selectivity of about 96% (Figure 4B), further demonstrating the similar surface PtZn ensemble of [$PtZn_4$] in these PtZn IMAs. When correlating C_3H_6 formation rates with the amounts of [$PtZn_4$] species, a linear relationship between them was observed (Figure 4C). Also, when the C_3H_6 formation rates were normalized by per mole [$PtZn_4$], PtZn IMAs with different Pt loadings showed a very similar C_3H_6 formation rate (mol C_3H_6/mmol [$PtZn_4$]/h) (Figure S40). Therefore, the surface [$PtZn_4$] ensembles in PtZn IMAs may be the key active site structures for PDH to propylene.

To further demonstrate the unique geometric and electronic structures of the single-atom Pt_1 site in [$PtZn_4$] ensembles, we further compared different [$PtZn_\delta$] (δ = 0–4) ensembles in other PtZn alloys and [PtM_4] ensembles in other Pt_1M_1 (M = Fe, Co, Ni) IMAs. First, from the perspective of geometric structure, we prepared different PtZn alloys by exposing different [$PtZn_\delta$] (δ = 0–4) surface ensembles. As XRD patterns shown in Figure S41, the samples of Pt/SiO_2, Pt_3Zn/SiO_2, and Pt_1Zn_1/SiO_2 were successfully prepared, corresponding to the standard Pt (PDF#04-0802), Pt_3Zn alloy (PDF#06-0584), and Pt_1Zn_1 IMA (PDF#06-0604), respectively. On the

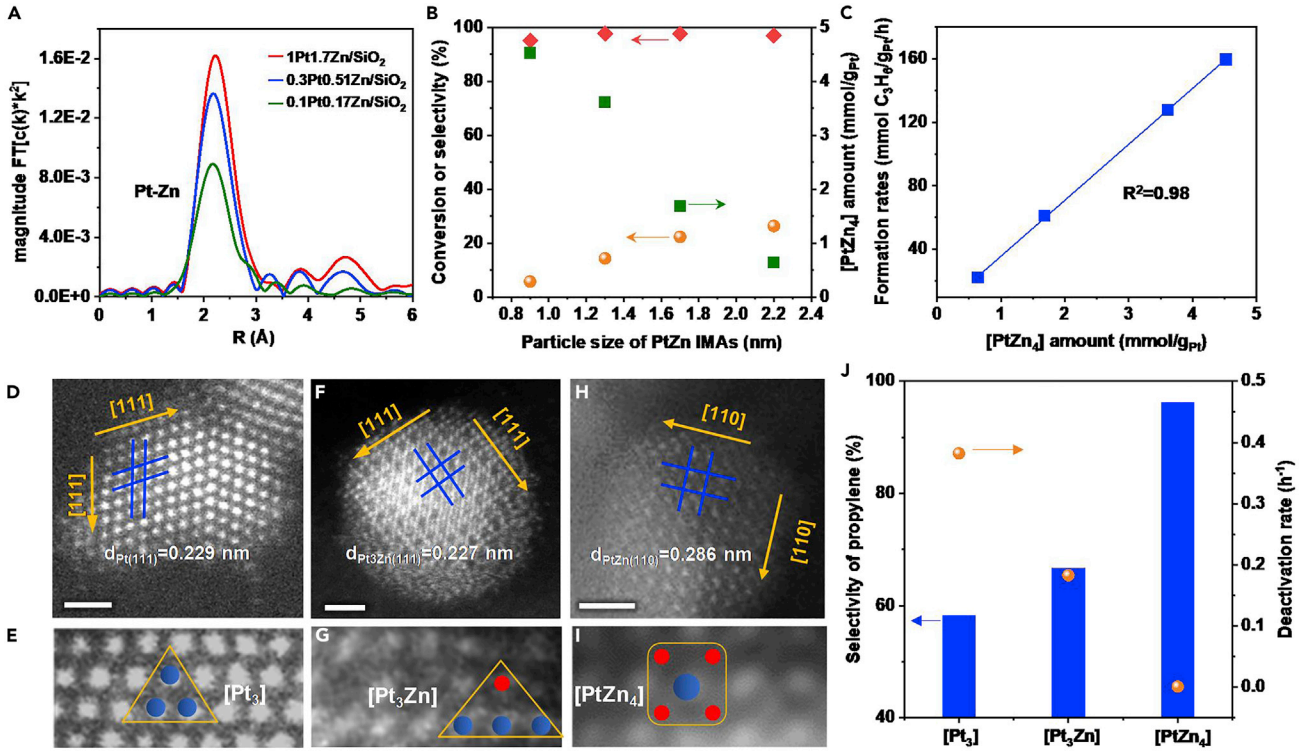

Figure 4. Quantitation of [PtZn$_4$] Amount and Comparison with Different [PtZn$_\delta$] (δ = 0–4) and [PM$_4$] Ensembles (M =F e, Co, Ni)

(A) *In situ* Pt L_{III} edge XANES spectra of different PtZn/SiO_2 IMAs.

(B) Conversion, selectivity, and [PtZn$_4$] amount as a function of PtZn IMA particle sizes in different PtZn/SiO_2 samples.

(C) Relationship of propylene formation rates and amounts of [PtZn$_4$]. Catalytic conditions: 600°C, atmospheric pressure, C_3H_8/H_2 = 1/1, with balance N_2 for a total flow rate of 50 mL min^{-1}, WHSV of propane = 200 h^{-1} and 5 mg of sample.

(D and E) AC-HAADF-STEM image of Pt/SiO_2. (the framed triangle represents the [Pt$_3$] ensemble).

(F and G) AC-HAADF-STEM image of Pt_3Zn/SiO_2. (the framed triangle represents the [Pt$_3$Zn] ensemble).

(H and I) AC-HAADF-STEM image of Pt_1Zn_1/SiO_2. (the framed rectangular represents the [PtZn$_4$] ensemble).

(the scale bar is 1 nm. Pt, blue; Zn, red).

(J) Comparison of propylene selectivity and deactivation rate over the ensembles of [Pt$_3$], [Pt$_3$Zn], and [PtZn$_4$].

Catalytic conditions: 600°C, atmospheric pressure, C_3H_8/H_2 = 1/1, with balance N_2 for a total flow rate of 50 mL min^{-1}, WHSV of propane = 4 h^{-1} and 250 mg of sample.

surface of these samples, different [PtZn$_\delta$] (δ = 0–4) ensembles formed, such as [Pt$_3$] on the surface of Pt (111) (Figures 4D and 4E), [Pt$_3$Zn] on the surface of Pt_3Zn (111) (Figures 4F and 4G), and [PtZn$_4$] on the surface of Pt_1Zn_1 (110) (Figures 4H and 4I). When testing for PDH reaction, we found that [PtZn$_4$] ensembles in Pt_1Zn_1 (110) IMA exhibited highest propylene selectivity among different [PtZn$_\delta$] (δ = 0–4) ensembles ([Pt$_3$] < [Pt$_3$Zn] < [PtZn$_4$]) (Figure 4J). This may be because of the fact that the geometry-isolated Pt_1 site in [PtZn$_4$] ensembles weaken the interaction between propylene intermediate and its surface through a single bond instead of more stable three Pt–C interactions on a 3-fold hollow site over [Pt$_3$] in Pt (111) and [Pt$_3$Zn] in Pt_3Zn (111). Additionally, to illustrate the unique electronic structures of this [PtZn$_4$] ensemble, we further compared the [PtZn$_4$] ensemble with other [PtM$_4$] ensembles in intermetallic Pt_1M_1 (M =F e, Co, Ni). As shown in Figure S42A, although their geometric structures were similar to that of [PtM$_4$] (M = Zn, Fe, Co, Ni) ensembles, where Pt atom is isolated by 4 neighboring M atoms on the surface of Pt_1M_1 IMAs, the electronic states significantly varied. Among them, Pt atoms in Pt_1Zn_1 IMAs exhibited higher electronic density due to more electron transfer from the neighboring Zn atoms than other atoms in the ensembles of [PtM$_4$] (M = Zn, Fe,

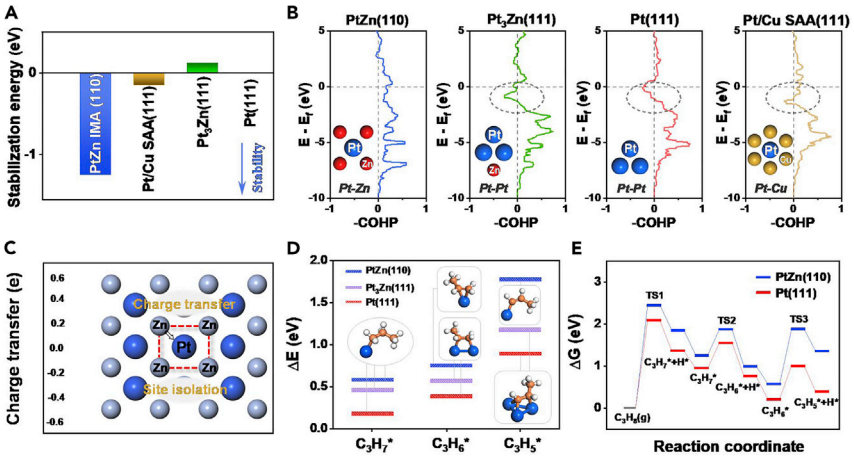

Figure 5. Density Functional Theory Calculations

(A) Stability of close-packed surfaces of PtZn IMA, Pt/Cu SAA, Pt_3Zn, and Pt.

(B) COHP curves. The Fermi level is at 0 eV. Gray dotted circle refers to antibonding interaction.

(C) Charge transfer is drawn at intervals of 0.2 and color-coded between −0.6 to 0.6.

(D) The adsorption geometries and energies of C_3H_x ($x = 7, 6, 5$). Color: Pt, blue; C, orange; H, white.

(E) The Gibbs free energy diagrams of PDH on PtZn (110) and Pt (111).

All the intermediates with (*) refer that they adsorb on the surfaces.

Co, Ni). As shown in Table S10, although the adsorption configuration of C_3H_6 on the top site of isolated Pt atom was similar, the adsorption energies of C_3H_6 significantly vary, where the adsorption strength of C_3H_6 were weakened in the order of $[PtNi_4]$ > $[PtCo_4]$ > $[PtFe_4]$ > $[PtZn_4]$. Consequently, the C_3H_6 selectivity increased in the order of $[PtNi_4]$ < $[PtCo_4]$ < $[PtFe_4]$ < $[PtZn_4]$ (Figure S42B). Therefore, the isolated Pt atom in $[PtM_4]$ ensembles is active for propane activation, but the neighboring coordination atoms significantly influence the electronic states of isolated Pt atom, wherein electron-richer single-atom Pt_1 site in $[PtZn_4]$ coordination ensembles accounts for higher propylene selectivity.

Therefore, by correlating the concentrations of $[PtZn_4]$ species with propylene formation rates and comparing $[PtZn_4]$ with different $[PtZn_\delta]$ (δ = 0–4) ensembles in PtZn alloys and $[PtM_4]$ (M = Fe, Co, Ni) in Pt_1M_1 IMAs, we reasonably prove that $[PtZn_4]$ ensembles in Pt_1Zn_1 (110) IMAs serve as the key active site structures. The induced geometry-isolated and electron-rich Pt in $[PtZn_4]$ ensembles could weaken the propylene adsorption and inhibit the structure-sensitive further dehydrogenation of propylene, leading to increased propylene selectivity and stability.

Density Functional Theory Calculations

We further carried out first-principle calculations to investigate the geometric and electronic promotions of this $[PtZn_4]$ ensembles for PDH. First, a DFT-based genetic algorithm (GA) was used to determine the global minimum (GM) structure of PtZn alloys, which indicated the atomically ordered IMA was the most stable phase among all the studied structures with a molar ratio of Pt:Zn = 1:1 (Figures S43–S45). DFT calculations further indicated that Pt_1Zn_1 (110) IMAs exhibited superior structural stability evaluated by surface segregation with the stabilization energy of <−1.0 eV compared with Pt (111) (0 eV), Pt_3Zn (111) (0.12 eV), and the previously reported Pt/Cu SAC (−0.15 eV) (Figure 5A).[7] The crystal orbital Hamilton population (COHP) analysis showed that there was the nonexistence of antibonding interaction in the region of −2 to 0 eV, below the Fermi level, which states the origin of structural steadiness of $[PtZn_4]$ ensembles in Pt_1Zn_1 (110) IMAs (Figure 5B).

A simplified reaction network was used to describe the dehydrogenation behavior (Figure S46). The first dehydrogenation step, considered to be the rate-determining step, measured the activity, and the difference between the third dehydrogenation step and propylene desorption barriers denotes the selectivity.[34] The transformation of adsorption geometries of dehydrogenated intermediates C_3H_x (x = 7, 6, 5) illustrates the critical discrepancy between [Pt_3], [Pt_3Zn], and [$PtZn_4$] ensembles (Figures 5D and S47). Specifically, owing to the site-isolated Pt_1 in [$PtZn_4$] ensembles, C_3H_5, a model precursor of coke formation, can only contact with its surface through a single bond instead of more stable three Pt–C interactions on a 3-fold hollow site over Pt_3 sites in Pt (111) and Pt_3Zn (111). The calculated charge transfer from the neighboring Zn to Pt (Table S8) further reveals the feature of electron enrichment of site-isolated Pt in [$PtZn_4$] ensembles (Figure 5C), which is beneficial to lower adsorption energy of propylene (Table S9). Consequently, compared with Pt (111) (< 0.1 eV), PtZn (110) IMA shows a larger difference between the third dehydrogenation step and propylene desorption barriers (> 1.0 eV), which leads to a much higher propylene selectivity and less coking favorability (Figures 5E and S48).

DISCUSSION

In conclusion, all the above simulations and experiments, taken together, persuasively evidence that atomically ordered PtZn IMAs are highly efficient for PDH. The unique geometric and electronic structures of surface [$PtZn_4$] ensembles effectively activate the first and second C–H bonds of propane but prohibit the structure-sensitive coke side reaction. The site-isolated Pt in [$PtZn_4$] ensembles can only contact with C_3H_5 through a single bond instead of more stable three Pt–C interactions in [Pt_3] ensembles, and the electron-rich Pt further promotes the desorption of propylene. Additionally, the atomically ordered IMA structure particularly guarantees the superior anti-segregation and anti-sintering resistance. The resulting single-site [$PtZn_4$] intermetallic catalysts bring the highest propylene productivity at a lowest deactivation rate under the industrial conditions. These findings provide a promising route to prepare efficient Pt-based bimetal dehydrogenation catalysts by isolating Pt atoms into single-site catalysts via assembling atomically ordered IMAs. We also expect that the reported discovery will open the exploitation of single-site IMAs as robust active sites for the catalytic dehydrogenation reactions as well as processing CO_2, N_2, and other carbonaceous fuels.

EXPERIMENTAL PROCEDURES

Resource Availability

Lead Contact

Further information and requests for resources and reagents should be directed to and will be fulfilled by the Lead Contact, Jinlong Gong (jlgong@tju.edu.cn).

Materials Availability

All unique/stable reagents generated in this study are available from the Lead Contact with a completed Materials Transfer Agreement.

Data and Code Availability

This study did not generate or analyze datasets or code.

Catalyst Preparation

All the catalysts were prepared by the incipient wetness impregnation method. $H_2PtCl_6 \cdot 6H_2O$ (Chemart (Tianjin) Chemical Technology Co., Ltd, 99.9%) and $Zn(NO_3)_2 \cdot 6H_2O$ (Aladdin (China) Chemical Co., Ltd, 98.0%) were mixed and used as precursors and amorphous SiO_2 (Alfa Aesar, 350–410 m^2/g, −325 mesh) was used as

support. $MgAl_2O_4$ supports were prepared by hydrolysis of aluminum isopropoxide (98%, Alfa Aesar) with $Mg(NO_3)_2 \cdot 6H_2O$ (98%, Alfa Aesar) in ethanol, as reported in the reference.[35] Then, ethanol was evaporated and the resultant gel was dried at 90°C overnight. Finally, the dried powders were calcined in ambient air at 800°C for 12 h with a heating rate of 5°C/min, resulting in the formation of $MgAl_2O_4$ support materials.

After impregnation, the catalysts were placed statically overnight and dried at 80°C for 12 h and then calcined at 600°C and 10% H_2-Ar atmosphere for 1.5 h. The metal loading is based on the weight ratio between metal and SiO_2, named as Pt/SiO_2 and $PtZn/SiO_2$ with 0.1 wt % feeding of Pt. *x* and *y* in xPt/SiO_2 and $xPtyZn/SiO_2$ means the feeding of Pt is *x* wt % and Zn is *y* wt %. Considering the loss of Zn atoms during H_2 reduction at HT, the ratios of $Zn(NO_3)_2 \cdot 6H_2O$ and $H_2PtCl_6 \cdot 6H_2O$ are determined to be more than 1. Al_2O_3 supported catalysts were prepared with the similar methods. Disordered PtZn catalyst was prepared at 300°C and 10% H_2-Ar atmosphere for 1 h. Zn/SiO_2 was prepared with $Zn(NO_3)_2 \cdot 6H_2O$ (Aladdin (China) Chemical Co., Ltd, 98.0%) and calcined at 600°C and 10% H_2-Ar atmosphere for 1.5 h.

The incipient wetness impregnation method was utilized to synthesize Al_2O_3 supported Pt–Sn (mimic Oleflex from UOP) catalysts to compare our PtZn IMA catalyst to the commercialized catalysts. For $PtSn/Al_2O_3$ reference catalysts, 0.5 wt % Pt, 1.5 wt % Sn, and 0.8 wt % K were utilized with $H_2PtCl_6 \cdot 6H_2O$ (Chemart (Tianjin) Chemical Technology Co., Ltd, 99.9%) and $SnCl_4 \cdot 5H_2O$ (Aladdin (China) Chemical Co., Ltd). (*13, 23*) The catalysts were dried for 2 h at 60°C and overnight at 120°C, followed by calcination at 560°C for 3 h. Pt/Cu SAA catalysts were prepared with $H_2PtCl_6 \cdot 6H_2O$ (Chemart (Tianjin) Chemical Technology Co., Ltd, 99.9%) and $Cu(NO_3)_2 \cdot 3H_2O$ (Alfa Aesar (China) Chemical Co., Ltd, 99.0%) and γ-Al_2O_3 (Sinopharm Chemical Reagent Co., Ltd, 98.0%) support. (*3*) After impregnation, the catalysts were placed statically overnight and dried at 80°C for 12 h and then calcined at 600°C for 2 h. The metal loading is based on the weight ratio between metal and γ-Al_2O_3, where 0.1 wt% Pt and 10 wt% Cu were obtained.

Catalytic Reaction Test

Catalytic tests were performed in a quartz fixed-bed reactor with an 8 mm inner diameter and 24 cm length at atmosphere pressure. 250 mg of the calcined catalyst with a particle size of 20 to 40 meshes was packed inside the quartz tubular reactor. The sample was first heated to 600°C at a rate of 10°C min^{-1} and retained at 600°C for 1.5 h in flowing 18 vol % H_2/N_2. During the activity test, a mixture of C_3H_8 (Air Liquide, 99.9%), H_2 (Air Liquide, 99.9%) and N_2 (Air Liquide, 99.9%) (16:16:68 vol %) was fed at a rate of 50 mL min^{-1} over 0.25 g catalysts. The WHSV of propane was around 4 h^{-1}. The stability test was performed under industrial operating conditions at 600°C, where a mixture of C_3H_8 (Air Liquide, 99.9%) and H_2 (Air Liquide, 99.9%) (67:33 vol %, no inert gas dilution) was fed at a rate of 12 mL min^{-1} over 0.1 g catalysts. The WHSV of propane was around 11 h^{-1}. The gas products were analyzed by an online GC (2060) equipped with a flame ionization detector (chromosorb 102 column) and a thermal conductivity detector (Al_2O_3 plot column). The propane conversion and selectivity to propylene were calculated from Equation 1 and 2, respectively. The propylene productivity is defined as the moles of C_3H_6 formation per g Pt per hour from Equation 3:

$$\text{Con}\ (\%) = 100 \times ([F_{C3H8}]_{inlet} - [F_{C3H8}]_{outlet}) / [F_{C3H8}]_{inlet}. \quad \text{(Equation 1)}$$

$$\text{Sel}\ (\%) = 100 \times [F_{C3H6}]_{outlet} / ([F_{C3H8}]_{inlet} - F_{C3H8}]_{outlet}) \quad \text{(Equation 2)}$$

$$\text{Productivity} = [F_{C3H6}]_{outlet} / (22.4 \cdot m_{cat} \cdot w_{Pt}) \quad \text{(Equation 3)}$$

where $[F_{C3H8}]$ and $[F_{C3H6}]$ mean mole flow rate of propane and propylene. m_{cat} is the weight of catalysts and W_{Pt} is the weight percent of Pt supported on the sample.

A first-order deactivation model was used to evaluate the catalyst stability:

$$k_d = (\ln [(1 - X_{final})/X_{final}] - \ln [(1 - X_{initial})/X_{intial}])/t \quad \text{(Equation 4)}$$

where X_{intial} and X_{fianal}, respectively, represent the conversion measured at the initial and final period of an experiment, and t represents the reaction time (h), k_d is the deactivation rate constant (h^{-1}). High k_d value means rapid deactivation, that is, low stability.

Methods for Characterization

The elemental composition of the catalysts was analyzed by inductively coupled plasma optical emission spectroscopy (ICP-OES) (VISTA-MPX, Varian). Before measurements, the catalysts were digested in the mixed solutions of hydrofluoric acid and aqua regia.

The XRD measurements were performed on a Bruker D8 diffractometer operating at 200 mA and 40 kV, employing the graphite filtered Cu Kα as the radiation source. The data points were collected by step scanning with a rate of 6° min^{-1} from 2θ = 10° to 80°. The crystallite size (*d*) of copper was calculated by X-ray broadening technique using the Scherrer's equation:

$$d = 0.89\ \lambda/(B \cos\theta) \quad \text{(Equation 5)}$$

Here, λ is the wavelength of the radiation source (0.15418 nm); B is the half-width of the strongest diffraction peak in the radian unit; and θ is its diffraction angle.

H_2-O_2 titration method was used to determine the dispersion of Pt with a Micromeritics AutoChem II 2920 apparatus with a thermal conductive detector based on our prior works. For every test, 100 mg of sample was reduced at 600°C with a flow rate of 30 mL min^{-1} of 10 vol % H_2/Ar for 1h, and then cooled down to 50°C under Ar purging. Subsequently, 10 vol % O_2/He was introduced to the sample by injection pulses until the consumption peaks became stable. Finally, H_2 chemisorption was performed by injection pulses of 10 vol % H_2/Ar. It can be presumed that the adsorption stoichiometry factor of Pt/H_2 was equal to 2/3. The platinum dispersion is calculated by the following equation:

$$\text{Dispersion (\%)} = 100 \times V_{H2} \times 2/3 \times MW_{Pt}/(W_{Pt} \times 22414) \quad \text{(Equation 6)}$$

where V_{H2} is the volume of adsorbed H_2 (mL), MW_{Pt} is the atomic weight of Pt ($g \cdot mol^{-1}$), and W_{Pt} is the weight of Pt supported on the sample (g).

TOF was calculated as moles of propane converted and propylene formed per mole of exposed Pt per second:

$$TOF = R_{C3H8\ (C3H6)}/D_{Pt} \quad \text{(Equation 7)}$$

where $R_{C3H8\ (C3H6)}$ is the specific activity of propane converted and propylene formation (s^{-1}); and D_{Pt} is the dispersion of Pt.

TEM was carried out on a JEM-2100F transmission electron microscope under a working voltage of 200 kV. The aberration-corrected scanning transmission electron microscopy (AC-STEM) images were characterized on FEI Titan Cubed Themis G2 300 (FEI) 200 kV, capable of sub-angstrom resolution at Tianjin University of Technology. The sample powder was dispersed in deionized water by ultrasonic and deposited on a cooper grid coated with an ultrathin holey carbon film.

The diffused reflectance infrared Fourier transform spectroscopy (CO-DRIFTS) of the catalysts were obtained by Nicolet 6700 spectrometer with a stainless-steel cell connected to a gas-dosing and evacuation system. 30 mg of the catalysts was compressed into *in situ* cell equipped with ZnSe windows. Prior to CO adsorption, the sample was reduced in H_2 with the flow rate is 30 mL/min at 600°C for 1.5 h. After that, the catalysts were purged under a flow of Ar (20 mL/min) for 0.5 h to remove the chemisorbed other impurity species and then cooled to 30°C under He to collect the background spectrum. Then the catalysts were exposed to a flow of a gas mixture of CO 3 mL/min, Ar 20 mL/min at 30°C for 0.5 h to adsorb CO, and then purging Ar (20 mL/min) for 20 min. The IR spectra can be collected with a resolution of 8 cm^{-1}.

In situ XPS analysis has been performed in ThermoFischer ESCALAB 250Xi photoelectron spectrometer using monochromated X-ray irradiation AlKα (hv = 1,486.7 eV) and 180° double-focusing hemispherical analyzer with a six-channel detector. The BE of the photoemission spectra was calibrated to Si 2p peak with BE 103.5 eV. After this calibration, the low intense adventitious carbon peak was in the range 284.0–284.8 eV. Reduction of samples was performed in an UHV connected high-pressure gas cell. The samples were heated in 10% hydrogen diluted in Ar (1 mL/min H_2 and 9 mL/min Ar, total pressure 1 bar) flow to 600°C for 60 min for reducing and then switch to 10% C_3H_8 diluted in He with 40 mL/min. The photoelectron spectra were recorded after UHV transfer of the samples to the analyzer chamber without contact with the atmosphere.

In situ Platinum L_3 edge and zinc K edge, X-ray adsorption spectroscopy (XAS) was measured at 10-BM (MRCAT) of the Advanced Photon Source, Argonne National Laboratory. Samples measured in transmission mode were ground into a fine powder and pressed into a stainless-steel sample holder and treated inside of a quartz tube reactor fitted with valves for gas flow and X-ray transparent Kapton windows. Samples were heated to 600°C in 3.5% H_2 (balance He) for 30 min. For the reaction condition treatments, samples were treated at 600°C with 3.5% H_2 and 3.5% C_3H_8 (balance He). The reactor was purged with helium at high temperature for 5 min before cooling to room temperature in helium for analysis. Helium used was ultra-high purity grade and was passed through an oxygen trap prior to use. Samples for fluorescence were ground into a fine powder and pressed into a stainless-steel sample holder with the catalyst wafer oriented 45° relative to the X-ray beam. The cell used for fluorescence measurement consists of a water-cooled stage fitted with Kapton windows for fluorescence and transmission measurement. For treatments, the cell is equipped with water cooling and ceramic heaters for temperature control and valves for gas flow.

For the Pt and Pt–Zn samples fluorescence was measured using a standard 3.3 cm Lytle detector with a Zn foil used to reduce background fluorescence. Fluorescence X-rays diffract through the logarithmically bent crystal and are angularly dispersed downstream of the crystal. By choosing the correct detector angle relative to the bent crystal, the Pt Lα fluorescence line was selectively collected. Data analysis

and fitting of the EXAFS was performed using WinXAS 3.1 software. XANES edge energy was taken as the first zero crossing of the second derivative of the normalized spectra. For the Pt–Zn samples data was Fourier transformed over k range of 2.7–10 $Å^{-1}$ and fit using from 1.3–3 Å in R space. Monometallic Pt samples were Fourier transformed over a k range of 2.7–14 $Å^{-1}$ and fit in R space from 1.9–3.1 Å. Pt–Pt phase and amplitude functions were extracted from Pt foil (12 neighbors 2.77 Á). Pt–Zn phase and amplitude functions were constructed using FEFF with the amplitude reduction factor, Debye-Waller factor, and E0 correction for the reference fixed at the value used to fit the platinum foil so that fit values of the Debye-Waller factor and E0 correction are relative to the platinum foil. The Pt–Zn bond distance was taken from ICSD data for the Pt_1Zn_1 phase with a Pt–Zn bond distance of 2.66 Å. Fitting was accomplished by first fixing the Debye-Waller factor and refining the coordination number, bond distance, and E0 correction in R space. The bond distance and E_0 were then fixed and the first shell scattering was isolated and back Fourier transformed into k space. The Debye-Waller factor and coordination number were then refined simultaneously on in R space and the isolated k space first shell scattering. For Pt–Zn samples, a model of the Pt_1Zn_1 phase was constructed by constraining the coordination number ratio of Pt–Zn: Pt–Pt neighbors to match that found in bulk Pt_1Zn_1 which has 8 zinc neighbors and 4 Pt neighbors giving a coordination number ratio of 2.

Temperature-programmed experiments were all carried out with a Micromeritics AutoChem 2920 apparatus. For O_2-TPO tests, 100 mg of samples after 10 h test at 600°C was heated at 300°C for 1 h and cooled down to 50°C in a flow of Ar (30 mL/min) and then heated in a stream of 10 vol % O_2/He (30 mL/min) with 10°C min^{-1} up to 800°C. For C_3H_8-TPSR tests, 100 mg of sample was heated at 300°C for 1 h and cooled down to 50°C in a flow of Ar (30 mL/min) and then reduced in a stream of C_3H_8 (5 mL/min) at a heating rate of 10°C min^{-1} up to 650°C. The output products (C_3H_8, C_3H_6, CH_4, and H_2, m/e equals 29, 41, 16, and 2, respectively) for both C_3H_8-TPSR were measured via mass spectrometer (MS) instantaneously. For C_3H_6-TPD experiments, 100 mg of sample was first reduced in flowing 10 vol % H_2/Ar at 600°C for 1 h. Then, the sample was cooled down to 50°C and the gas was switched to flowing Ar to flush the apparatus. Subsequently, the adsorption of C_3H_6 was achieved by the introduction of flowing C_3H_6 for 45 min, and then the system was purged with flowing He for 30 min. After that, the sample was raised at a rate of 10°C/min up to 600°C in flowing He.

DFT Calculations

All periodic boundary calculations were carried out with the Vienna *ab initio* Simulation Package (VASP) using the projector augmented wave (PAW) method and the generalized gradient approximation (GGA) in the form of the Bayesian error estimation functional with van der Waals corrections (BEEF-vdW). The plane-wave basis set was converged at a cutoff energy of 400 eV for each slab model, of which the bottom two layers were fixed. A four-layer 4 × 4 unit cell and a five-layer 2 × 2 unit cell were used for Pt (111) and PtZn (110), respectively. The k-points mesh of 3 × 3 × 1 was used. All structures were allowed to relax until the force on each atom was less than 0.02 eV/Å. Transition states (TSs) were determined with the climbing-image nudged elastic band (CI-NEB) method or the dimer method. The computational method is the same as Chen et al.,[36] in order to make reliable contrast.

Entropic contributions and zero-point energy (ZPE) were taken into account, converting DFT calculated energy into free energy. According to Campbell's method,[37] the entropy of adsorbate was calculated with the equation as follows:

$$S_{ads} = 0.7S_{gas} - 3.3R \quad \text{(Equation 8)}$$

where S_{ads} is the entropy of adsorbate; S_{gas} is the entropy of the corresponding gas-phase species, which can be generally obtained from a standard thermodynamic database, using the heat capacity to extrapolate to unlisted temperatures; and R is the ideal gas constant. No entropy change is assumed for surface reaction as the harmonic approximation is poor at determining entropy in low-frequency vibrational modes. All the kinetic and thermodynamic analyses were carried out at 873 K with 0.28, 0.15, and 0.04 atm partial pressures for H_2, C_3H_8 and C_3H_6, respectively, which kept pace with the experimental conditions.

The adsorption energy is defined as $E_{total} - E_{slab} - E_{C3H8} + [(8 - x)/2]E_{H2}$, where E_{total} is the total energy of the slab with C_3H_x adsorbed, E_{slab} is the energy of clean slab while E_{C3H8} and E_{H2} refer to the energy of C_3H_8 and H_2 in the gas phase, respectively.

The alloy formation energy, −1.1 eV for PtZn IMA, is characterized by bulk energy of alloy and pure metal with the same number of atoms, namely, $\Delta E = E_{PtZn} - E_{Pt} - E_{Zn}$. Here, a negative value indicates that alloy formation is energetically favorable, in accordance with the large miscibility of Pt with Zn to experimentally examine alloys.

The surface energy, γ, is calculated with the following formula:

$$\gamma = \frac{1}{2A}\left[E_{slab}^{unrelax} - n\,E_{bulk}\right] + \frac{1}{2A}\left[E_{slab}^{relax} - E_{slab}^{unrelax}\right] \quad \text{(Equation 9)}$$

E_{bulk}: Energy of a single unit in bulk. $E_{slab}^{unrelax}$: Single point energy of the slab model. E_{slab}^{relax}: Energy of the slab model. A, surface area of the slab model; n, number of units in the slab model

Moreover, as Zn with the lower surface energy manifests stronger segregation propensity than Pt, the surface segregation of Zn is further investigated to elucidate the stability of Zn in PtZn IMA. The stabilization energy of Zn is −0.66 eV, which states the segregation of Zn is unfavorable in PtZn. In addition, based on the nearest-neighbor approximation and calculated cohesive energies,[37] one estimates the following bond energies: E_{Zn-Zn} = −0.18 eV, E_{Pt-Pt} = −0.46 eV and E_{Pt-Zn} = −0.49 eV. The energy change due to the formation of one Pt–Zn bond from Pt–Pt and Zn–Zn bonds is: $-0.49 - [(-0.18) + (-0.46)]/2 = -0.17$ eV. This negative energy change implies that the formation of Pt–Zn bond is exothermic, which can oppose Zn segregation in an alloy through releasing energy. However, it is still necessary to clarify whether the exothermic alloy formation is able to overcome the surface segregation of Zn. For alloy (A+B), surface enrichment takes place in the component B with lower surface energy[38] while its segregation can be overcome by the formation of AB alloy when the inequality $EA_A > E_{AB}$ holds, where E_{AA} and E_{AB} are the bond energy between atoms of component A or between atoms of different components. For PtZn alloy, A = Pt and B = Zn. Based on the calculated bond energies, one can see that $E_{Pt-Pt} > E_{Pt-Zn}$, demonstrating that the energy gain by forming Pt–Zn bonds is sufficient to overcome the surface segregation of Zn in PtZn IMA.

SUPPLEMENTAL INFORMATION

Supplemental Information can be found online at https://doi.org/10.1016/j.chempr.2020.10.008.

ACKNOWLEDGMENTS

This work is supported by the National Science Foundation of China (21525626 and U1862207) and the Program of Introducing Talents of Discipline to Universities

(BP0618007). S.C.P. and J.T.M. were supported by the US National Science Foundation under cooperative agreement no. EEC-1647722. This research used resources from the Advanced Photon Source, a US Department of Energy (DOE) Office of Science user facility operated for the DOE Office of Science by Argonne National Laboratory under contract no. DE-AC02-06CH11357. MRCAT (APS/10-BM) operations are supported by the Department of Energy and the MRCAT member institutions. A.J.K. gratefully acknowledges support from the US DOE, Office of Basic Energy Sciences, Division of Chemical Sciences, Geosciences, and Biosciences, Catalysis Science Program under contract DE-AC-02-06CH11357.

AUTHOR CONTRIBUTIONS

J.G. conceived and coordinated the research. S.C. contributed to catalyst synthesis and catalytic experiments. S.C. and G.S. performed DRIFTS experiments, TPSR, and long-term stability experiments. J.L. collected and analyzed the AC-HAADF-STEM data. S.C.P., A.J.K., and J.T.M. performed the EXAFS measurements and analyzed the data. X.C. and Z.-J.Z. screened PtZn IMA catalyst by DFT. S.C., Z.-J.Z., X.C., R.M., and J.G. wrote the manuscript. All authors participated in discussion of the research.

DECLARATION OF INTERESTS

The authors declare no competing interests.

Received: May 22, 2020
Revised: July 6, 2020
Accepted: October 9, 2020
Published: November 4, 2020

REFERENCES

1. Sattler, J.J., Ruiz-Martinez, J., Santillan-Jimenez, E., and Weckhuysen, B.M. (2014). Catalytic dehydrogenation of light alkanes on metals and metal oxides. Chem. Rev. *114*, 10613–10653.

2. Grant, J.T., Carrero, C.A., Goeltl, F., Venegas, J., Mueller, P., Burt, S.P., Specht, S.E., McDermott, W.P., Chieregato, A., and Hermans, I. (2016). Selective oxidative dehydrogenation of propane to propene using boron nitride catalysts. Science *354*, 1570–1573.

3. Chen, S., Zeng, L., Mu, R., Xiong, C., Zhao, Z.J., Zhao, C., Pei, C., Peng, L., Luo, J., Fan, L.-S., and Gong, J. (2019). Modulating lattice oxygen in dual-functional Mo-V-O mixed oxides for chemical looping oxidative dehydrogenation. J. Am. Chem. Soc. *141*, 18653–18657.

4. Liu, G., Zhao, Z.-J., Wu, T., Zeng, L., and Gong, J. (2016). Nature of the active sites of VO_x/Al_2O_3 catalysts for propane dehydrogenation. ACS Catal *6*, 5207–5214.

5. Xiong, H., Lin, S., Goetze, J., Pletcher, P., Guo, H., Kovarik, L., Artyushkova, K., Weckhuysen, B.M., and Datye, A.K. (2017). Thermally stable and regenerable platinum-tin clusters for propane dehydrogenation prepared by atom trapping on ceria. Angew Chem Int Ed Engl *56*, 8986–8991.

6. Hu, Z.-P., Yang, D., Wang, Z., and Yuan, Z.-Y. (2019). State-of-the-art catalysts for direct dehydrogenation of propane to propylene. Chin. J. Catal. *40*, 1233–1254.

7. Sun, G., Zhao, Z.J., Mu, R., Zha, S., Li, L., Chen, S., Zang, K., Luo, J., Li, Z., Purdy, S.C., et al. (2018). Breaking the scaling relationship via thermally stable Pt/Cu single atom alloys for catalytic dehydrogenation. Nat. Commun. *9*, 4454.

8. Zhu, J., Yang, M., Yu, Y., Zhu, Y., Sui, Z., Zhou, X., Holmen, A., and Chen, D. (2015). Size-dependent reaction mechanism and kinetics for propane dehydrogenation over Pt catalysts. ACS Catal. *5*, 6310–6319.

9. Marcinkowski, M.D., Darby, M.T., Liu, J., Wimble, J.M., Lucci, F.R., Lee, S., Michaelides, A., Flytzani-Stephanopoulos, M., Stamatakis, M., and Sykes, E.C.H. (2018). Pt/Cu single-atom alloys as coke-resistant catalysts for efficient C-H activation. Nat. Chem. *10*, 325–332.

10. Qiao, B., Wang, A., Yang, X., Allard, L.F., Jiang, Z., Cui, Y., Liu, J., Li, J., and Zhang, T. (2011). Single-atom catalysis of CO oxidation using Pt1/FeOx. Nat. Chem. *3*, 634–641.

11. Wegener, E.C., Bukowski, B.C., Yang, D., Wu, Z., Kropf, A.J., Delgass, W.N., Greeley, J., Zhang, G., and Miller, J.T. (2020). Intermetallic compounds as an alternative to single-atom alloy catalysts: geometric and electronic structures from advanced X-ray spectroscopies and computational studies. ChemCatChem *12*, 1325–1333.

12. Li, Z., Yu, L., Milligan, C., Ma, T., Zhou, L., Cui, Y., Qi, Z., Libretto, N., Xu, B., Luo, J., et al. (2018). Two-dimensional transition metal carbides as supports for tuning the chemistry of catalytic nanoparticles. Nat. Commun. *9*, 5258.

13. Khorshidi, A., Violet, J., Hashemi, J., and Peterson, A.A. (2018). How strain can break the scaling relations of catalysis. Nat. Catal. *1*, 263–268.

14. Mehta, P., Barboun, P., Herrera, F.A., Kim, J., Rumbach, P., Go, D.B., Hicks, J.C., and Schneider, W.F. (2018). Overcoming ammonia synthesis scaling relations with plasma-enabled catalysis. Nat. Catal. *1*, 269–275.

15. Greiner, M.T., Jones, T.E., Beeg, S., Zwiener, L., Scherzer, M., Girgsdies, F., Piccinin, S., Armbrüster, M., Knop-Gericke, A., and Schlögl, R. (2018). Free-atom-like d states in single-atom alloy catalysts. Nat. Chem. *10*, 1008–1015.

16. Kyriakou, G., Boucher, M.B., Jewell, A.D., Lewis, E.A., Lawton, T.J., Baber, A.E., Tierney, H.L., Flytzani-Stephanopoulos, M., and Sykes, E.C. (2012). Isolated metal atom geometries as a strategy for selective heterogeneous hydrogenations. Science *335*, 1209–1212.

17. Wang, A., Li, J., and Zhang, T. (2018). Heterogeneous single-atom catalysis. Nat. Rev. Chem. *2*, 65–81.

18. Schweitzer, N.M., Hu, B., Das, U., Kim, H., Greeley, J., Curtiss, L.A., Stair, P.C., Miller, J.T., and Hock, A.S. (2014). Propylene

hydrogenation and propane dehydrogenation by a single-site Zn^{2+} on silica catalyst. ACS Catal. *4*, 1091–1098.

19. Hu, B., "Bean" Getsoian, A., Schweitzer, N.M., Das, U., Kim, H., Niklas, J., Poluektov, O., Curtiss, L.A., Stair, P.C., Miller, J.T., and Hock, A.S. (2015). Selective propane dehydrogenation with single-site Co^{II} on SiO_2 by a non-redox mechanism. J. Catal. *322*, 24–37.

20. Zhang, G., Yang, C., and Miller, J.T. (2018). Tetrahedral nickel(II) phosphosilicate single-site selective propane dehydrogenation catalyst. ChemCatChem *10*, 961–964.

21. Searles, K., Siddiqi, G., Safonova, O.V., and Copéret, C. (2017). Silica-supported isolated gallium sites as highly active, selective and stable propane dehydrogenation catalysts. Chem. Sci. *8*, 2661–2666.

22. Zhang, L., Zhou, M., Wang, A., and Zhang, T. (2020). Selective hydrogenation over supported metal catalysts: from nanoparticles to single atoms. Chem. Rev. *120*, 683–733.

23. Nakaya, Y., Hirayama, J., Yamazoe, S., Shimizu, K.I., and Furukawa, S. (2020). Single-atom Pt in intermetallics as an ultrastable and selective catalyst for propane dehydrogenation. Nat. Commun. *11*, 2838.

24. Cybulskis, V.J., Bukowski, B.C., Tseng, H., Gallagher, J.R., Wu, Z., Wegener, E., Kropf, A.J., Ravel, B., Ribeiro, F.H., Greeley, J., and Miller, J.T. (2017). Zinc promotion of platinum for catalytic light alkane dehydrogenation: insights into geometric and electronic effects. ACS Catal. *7*, 4173–4181.

25. Wang, Y., Hu, Z.-P., Lv, X., Chen, L., and Yuan, Z.-Y. (2020). Ultrasmall PtZn bimetallic nanoclusters encapsulated in silicalite-1 zeolite with superior performance for propane dehydrogenation. J. Catal. *385*, 61–69.

26. Sun, Q., Wang, N., Fan, Q., Zeng, L., Mayoral, A., Miao, S., Yang, R., Jiang, Z., Zhou, W., Zhang, J., et al. (2020). Subnanometer bimetallic platinum-zinc clusters in zeolites for propane dehydrogenation. Angew. Chem. Int. Ed. Engl. *59*, 2–11.

27. Qi, Z., Xiao, C., Liu, C., Goh, T.W., Zhou, L., Maligal-Ganesh, R., Pei, Y., Li, X., Curtiss, L.A., and Huang, W. (2017). Sub-4 nm PtZn intermetallic nanoparticles for enhanced mass and specific activities in catalytic electrooxidation reaction. J. Am. Chem. Soc. *139*, 4762–4768.

28. Shi, L., Deng, G., Li, W., Miao, S., Wang, Q., Zhang, W., and Lu, A. (2015). Al_2O_3 nanosheets rich in pentacoordinate Al^{3+} ions stabilize Pt-Sn clusters for propane dehydrogenation. Angew. Chem. Int. Ed. Engl. *54*, 13994–13998.

29. Han, Z., Li, S., Jiang, F., Wang, T., Ma, X., and Gong, J. (2014). Propane dehydrogenation over Pt-Cu bimetallic catalysts: the nature of coke deposition and the role of copper. Nanoscale *6*, 10000–10008.

30. Baria, O.A., Holmen, A., and Blekkan, E.A. (2018). Propane dehydrogenation over supported Pt and Pt–Sn catalysts: catalyst preparation, characterization, and activity measurements. J. Catal. *158*, 1–12.

31. Dvořák, F., Farnesi Camellone, M., Tovt, A., Tran, N.D., Negreiros, F.R., Vorokhta, M., Skála, T., Matolínová, I., Mysliveček, J., Matolín, V., and Fabris, S. (2016). Creating single-atom Pt-ceria catalysts by surface step decoration. Nat. Commun. *7*, 10801.

32. Yu, C., Xu, H., Ge, Q., and Li, W. (2007). Properties of the metallic phase of zinc-doped platinum catalysts for propane dehydrogenation. J. Mol. Catal. A *266*, 80–87.

33. Almutairi, S.M.T., Mezari, B., Magusin, P.C.M.M., Pidko, E.A., and Hensen, E.J.M. (2012). Structure and reactivity of Zn-modified ZSM-5 zeolites: the importance of clustered cationic Zn complexes. ACS Catal. *2*, 71–83.

34. Zha, S., Sun, G., Wu, T., Zhao, J., Zhao, Z.J., and Gong, J. (2018). Identification of Pt-based catalysts for propane dehydrogenation via a probability analysis. Chem. Sci. *9*, 3925–3931.

35. Li, W.Z., Kovarik, L., Mei, D., Liu, J., Wang, Y., and Peden, C.H. (2013). Stable platinum nanoparticles on specific $MgAl_2O_4$ spinel facets at high temperatures in oxidizing atmospheres. Nat. Commun. *4*, 2481.

36. Chen, Z.-X., Neyman, K.M., Gordienko, A.B., and Rösch, N. (2003). Surface structure and stability of PdZn and PtZn alloys:density-functional slab model studies. Phys. Rev. B *68*, 075417.

37. Campbell, C.T. (1990). Bimetallic surface chemistry. Annu. Rev. Phys. Chem. *41*, 775–837.

38. Campbell, C.T., Árnadóttir, L., and Sellers, J.R.V. (2013). Kinetic prefactors of reactions on solid surfaces. Z. Phys. Chem. *227*, 1435–1454.